

Multi-view Hybrid Graph Convolutional Network for Volume-to-mesh Reconstruction in Cardiovascular MRI

Nicolás Gaggion, Benjamin A. Matheson, Yan Xia, Rodrigo Bonazzola, Nishant Ravikumar, Zeike A. Taylor, Diego H. Milone, Alejandro F. Frangi, Enzo Ferrante

Abstract—Cardiovascular magnetic resonance imaging is emerging as a crucial tool to examine cardiac morphology and function. Essential to this endeavour are anatomical 3D surface and volumetric meshes derived from CMR images, which facilitate computational anatomy studies, biomarker discovery, and in-silico simulations. However, conventional surface mesh generation methods, such as active shape models and multi-atlas segmentation, are highly time-consuming and require complex processing pipelines to generate simulation-ready 3D meshes. In response, we introduce HybridVNet, a novel architecture for direct image-to-mesh extraction seamlessly integrating standard convolutional neural networks with graph convolutions, which we prove can efficiently handle surface and volumetric meshes by encoding them as graph structures. To further enhance accuracy, we propose a multiview HybridVNet architecture which processes both long axis and short axis CMR, showing that it can increase the performance of cardiac MR mesh generation. Our model combines traditional convolutional networks with variational graph generative models, deep supervision and mesh-specific regularisation. Experiments on a comprehensive dataset from the UK Biobank confirm the potential of HybridVNet to significantly advance cardiac imaging and computational cardiology by efficiently generating high-fidelity and simulation ready meshes from CMR images.

Index Terms—Cardiac Imaging, Geometric Deep Learning, Hybrid Graph Convolutional Neural Network, Volume-to-Mesh

N. Gaggion, D.H. Milone, and E. Ferrante are with the Institute for Signals, Systems, and Computational Intelligence, sinc(i) CONICET-UNL, Santa Fe, Argentina. (e-mails: ngaggion@sinc.unl.edu.ar, dmilone@sinc.unl.edu.ar, eferrante@sinc.unl.edu.ar).

B.A. Matheson, Y. Xia, R. Bonazzola, N. Ravikumar, and Z.A. Taylor are with the Centre for Computational Imaging and Simulation Technologies in Biomedicine (CISTIB), School of Computing, University of Leeds, Leeds, UK; A.F. Frangi is with the Christabel Pankhurst Institute, Division of Informatics, Imaging, and Data Sciences, School of Health Sciences, and the Department of Computer Science, School of Engineering, The University of Manchester, UK. He is also with the Medical Imaging Research Centre (MIRC), Department of Cardiovascular Sciences, and the Department of Electrical Engineering, KU Leuven, Leuven, Belgium. Finally, he is at the Alan Turing Institute, London, UK.

AFF acknowledges support from the Royal Academy of Engineering under the RAEng Chair in Emerging Technologies (INSILEX CiET1919/19) and the ERC Advanced Grant – UKRI Frontier Research Guarantee (INSILICO EP/Y030494/1).

EF acknowledges support from the Google Award for Inclusion Research program, Nvidia for the donation of GPU computing, the Argentinian Agencia Nacional de Promoción de la Investigación, el Desarrollo Tecnológico y la Innovación (PICT PRH 2019-0009), and Universidad Nacional del Litoral (CAID project).

I. INTRODUCTION

Cardiac imaging has undergone significant advances in recent years, becoming an indispensable tool in the diagnosis, treatment planning, and management of various cardiovascular diseases. One of the critical components of such advancements is the extraction of accurate 3D meshes from cardiovascular magnetic resonance (CMR) images, which serve as the basis for computational simulations [1], discovery of biomarkers [2], and analysis of hearth deformation and dynamics [3].

Despite the undeniable importance of cardiac mesh extraction, the task is fraught with challenges. Traditional methods, such as active shape models [4] and multi-atlas segmentation [5], often require extensive computational resources and can be time-consuming. The variability in heart shapes, sizes, and pathologies further complicates the extraction process, necessitating a robust and adaptable method.

Furthermore, transitioning from 2D image slices to a cohesive 3D representation demands a seamless integration of spatial information, especially when modelling tetrahedral meshes. Current methodologies often require intricate post-processing steps to refine the meshes [1], [6], making them suitable for simulations, which can introduce additional sources of error and prolong the overall processing time. In light of these challenges, there is a pressing need for innovative approaches that can streamline the cardiac mesh extraction process, improve accuracy, and reduce time and computational overhead. This paper introduces a novel method for generating high-quality surface and volumetric meshes, immediately suitable for computational models, directly from CMR imaging.

Generating detailed and anatomically plausible ventricular meshes from CMR images is challenging and time-consuming if performed manually. Automatic methods for mesh extraction are primarily dependent on the concatenation of several stages, usually including segmentation at the voxel level, surface mesh extraction, and a final step of volumetric mesh generation [1], [6]. One of the main limitations of these approaches is that voxel-level segmentation techniques (usually deep learning models such as the U-Net [7] or the volumetric V-Net [8]) are prone to introduce errors due to the local support of the convolutional models, resulting in unrealistic masks with holes or spurious segmentations [9]. Other approaches are based on

deforming an initial template. In that regard, previous studies have proposed to estimate the displacements of the mesh nodes [10], [11] or directly deform the space that surrounds a simulation-ready whole heart template [12]. However, the accuracy of these approaches is bounded by the quality of the estimated deformations.

Closer to our work, in [13], [14], a neural network is trained end-to-end to estimate parameterised shapes directly from images. These methods use convolutional neural networks to infer the parameters of a Principal Component Analysis (PCA) shape model. Despite the utility of PCA-based models in mesh extraction from volumetric images, their expressiveness is inherently limited by the linearity of PCA. To address this limitation, we enhance the expressiveness of parametric shapes by leveraging a graph-convolutional decoder capable of handling both surface and volumetric meshes. Previous studies have used generative models based on geometric deep learning [15], [16] to extract contours from 2D images. Our contribution builds on this foundation, introducing the HybridVNet architecture and its multiview variant. It combines standard 3D convolutions for volumetric image encoding with a decoder based on spectral graph convolutions for cardiac mesh generation.

Contributions: Our primary contributions encompass the development of a multiview volumetric hybrid graph convolutional model capable of seamlessly integrating multiple CMR views within a jointly learnt latent space, directly producing meshes from images. Our model exhibits a natural ability to create both cardiac surfaces and tetrahedral meshes, suited for finite element simulations. We further explore classic regularisation techniques for surface meshes and introduce a novel differentiable regularisation term specifically tailored for tetrahedral meshes, markedly enhancing element quality. Notably, while previous works often relied on cropped regions of volumetric images, our model demonstrates exceptional performance in both cropped areas and complete images. The performance of the model is rigorously evaluated using the UK Biobank CMR data set [17] ground truth annotations.

II. VOLUME-TO-MESH EXTRACTION IN CARDIOVASCULAR MR

A. Reference CMR meshes and images

The reference cohort of 3D surface meshes used in this study was introduced in Xia *et al.* (2022) [14]. It was created by registering a high-resolution atlas of the human heart [18] to manually delineate 2D contours at end-diastole (ED) and end-systole (ES). The rationale behind selecting the subjects chosen for manual segmentation and the methodology followed can be found in [19]. This atlas consists of a mesh that includes six separate structures: the left ventricle (LV), the right ventricle (RV), the left atrium (LA), the right atrium (RA), and the ascending aorta. Since the cohort was obtained by registering an atlas, note that each of the final ground-truth meshes has the same number of nodes and set of faces, giving the same adjacency matrix. More details about the image and surface mesh dataset are provided in Section III-A.

Volumetric mesh dataset generation: We derived volumetric mesh ground-truth annotations from the surface meshes. We used the one-to-one correspondence between surface nodes to register a volumetric atlas to the cardiac surface mesh dataset. The Simpleware software (Version Medical T-2022.03, Synopsis Inc., Mountain View, USA) [20] was used to construct the volumetric atlas mesh. We imported heart structures from the human heart atlas [18] as individual closed surface meshes of triangular elements. Then, we populated the hollow surface meshes with tetrahedral elements, setting the elements at the interfaces between different cardiac structures to share nodes. This resulted in a mesh of 408,764 elements. We registered the volumetric atlas on the entire surface dataset using mesh-to-mesh thin plate spline warping, using the Vedo library [21].

B. HybridVNet formulation

As shown in Figure 1, our HybridVNet model receives multiple CMR views as input: the short-axis view (SAX), which is a 3D cross-sectional view of the heart acquired perpendicular to the long axis, and three different 2D long-axis views (LAX), for two, three and four chambers of the heart (LAX 2CH, LAX 3CH and LAX 4CH, respectively), providing 2D cross-sectional views acquired parallel to the long axis. Given these four images (one volumetric and three 2D), we aim to generate a (surface or tetrahedral) mesh representing the structures of interest.

Consider a dataset $\mathcal{D} = \{(\mathbf{I}, \mathbf{G})_n\}_{0 < n \leq N}$, composed of N samples of multi-view CMR images $\mathbf{I} = (\mathbf{I}^{\text{LAX 2CH}}, \mathbf{I}^{\text{LAX 3CH}}, \mathbf{I}^{\text{LAX 4CH}}, \mathbf{I}^{\text{SAX}})$, and their associated cardiac meshes as graphs $\mathbf{G} = \langle V, \mathbf{A}, \mathbf{X} \rangle$, where V is the set of M nodes or vertices ($|V| = M$), $\mathbf{A} \in \{0, 1\}^{M \times M}$ is the adjacency matrix indicating the connectivity between pairs of nodes ($a_{ij} = 1$ indicates an edge connecting vertices i and j , and $a_{ij} = 0$ otherwise), and $\mathbf{X} \in \mathbb{R}^{M \times s}$ is a function (represented as a matrix) assigning a feature vector to every node. It assigns a 3-dimensional spatial coordinate (the mesh vertex position, $s = 3$). Since our dataset includes meshes with the same number of nodes and the same connectivity by construction, we can use spectral graph convolutions to decode meshes from a latent space [22], [2].

The proposed model consists of a hybrid variational encoder-decoder architecture with multiple inputs. An image convolutional encoder, learns a latent representation of the input images, and a spectral graph convolutional decoder generates a graph representation of the organ. Since our input consists of four images with varying shapes and views, we use a multiview encoder to handle it. To this end, independent encoder branches are defined for each image view, and a joint latent space is constructed by concatenating their outputs. For all types of LAX images, we use 2D convolutional encoders, $f_e^{\text{LAX 2CH}}$, $f_e^{\text{LAX 3CH}}$ and $f_e^{\text{LAX 4CH}}$, with residual convolutions [23]. For the 3D SAX image, we use a 3D convolutional encoder, f_e^{SAX} , consisting of 3D residual blocks interleaved by max-pooling operations.

Consequently, our model uses a variational encoder-decoder architecture to generate a graph representation of a desired organ from multiview input images. The encoder

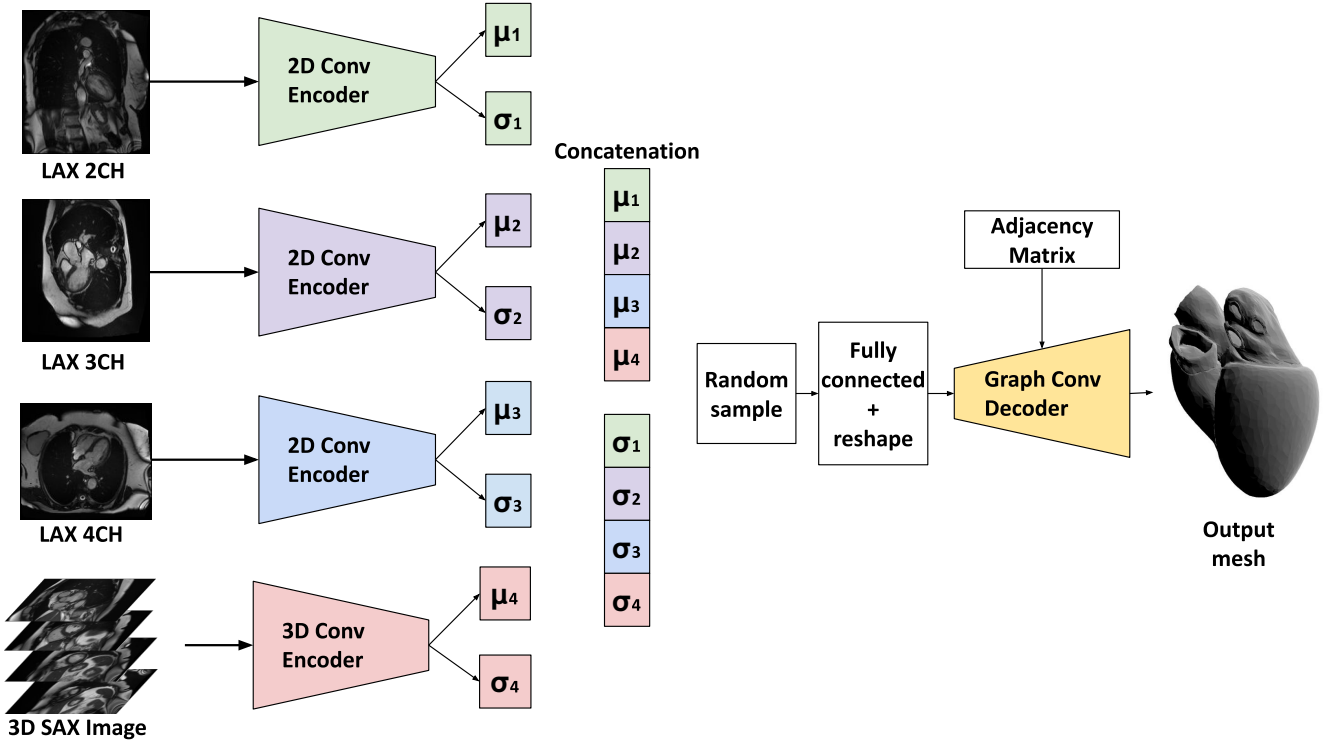


Fig. 1: Multiview HybridVNet model architecture: The proposed model uses a variational encoder-decoder architecture to generate a graph representation of a desired organ from multiview input images. The encoder consists of independent branches for each input view, concatenated to obtain a joint latent space. The latent code is then passed through a fully connected layer and reshaped to obtain the initial node features for the graph convolutional decoder. This decoder uses the initial node features to generate a final graph representation of the organ.

maps the input to a lower-dimensional embedding which represents the parameters of a latent distribution, $\mathbf{z} = f_e^I(\mathbf{I}^{\text{LAX 2CH}}, \mathbf{I}^{\text{LAX 3CH}}, \mathbf{I}^{\text{LAX 4CH}}, \mathbf{I}^{\text{SAX}})$. This latent distribution is then sampled using the reparametrisation trick [24], passed through a fully connected layer, and reshaped to obtain initial node features for the graph convolutional decoder, f_d^G . Following the variational autoencoder formulation, the latent code is assumed to be sampled from a multivariate Gaussian posterior, $Q(\mathbf{z}|\mathbf{I}) = \mathcal{N}(\boldsymbol{\mu}, \text{diag}(\boldsymbol{\sigma}))$. The distribution is parameterised by the concatenation of outputs from the joint multiview encoder, $(\boldsymbol{\mu}, \boldsymbol{\sigma}) = f_e^I(\mathbf{I})$. Given a sample of the latent code, \mathbf{z} , the graph representation of the organ can be obtained through the decoder $f_d^G(\mathbf{z})$.

The model is trained by minimising a loss function defined as

$$\mathcal{L} = \mathcal{L}_r(f_d(f_e(\mathbf{I})), \mathbf{G}) + \lambda_{KL} \mathcal{L}_{KL}(Q(\mathbf{z}|\mathbf{I})||\mathcal{N}(0, 1)), \quad (1)$$

where the first term is the reconstruction loss based on the mean squared error (MSE) of the vertex positions, the second term imposes a unit Gaussian prior $\mathcal{N}(0, 1)$ for the latent posteriors via the KL divergence loss (\mathcal{L}_{KL}) and λ_{KL} is a weighting factor.

Deeply-supervised spectral graph decoder: To generate the graph representation of the target organ, we employed a

decoder constructed using spectral graph convolutional neural networks (GCNN). Spectral convolutions are based on the eigendecomposition of the graph Laplacian matrix. In this context, we adopt the spectral convolutions introduced by Defferrard et al. (2016) [25], which constrain the filters to polynomial filters. This constraint arises from the observation that polynomial filters exhibit strict localisation in the vertex domain, consequently reducing the computational complexity of the convolutional operation. For an in-depth understanding of spectral convolutions, please refer to [25].

A spectral convolutional layer operates as standard convolutions applied to images and feature maps. It takes an input feature matrix \mathbf{X}^ℓ and produces filtered versions $\mathbf{X}^{\ell+1}$ as output. Our spectral decoder architecture comprises five graph-convolutional layers, each complemented by ReLU nonlinearities with previous Layer Normalisation [26]. These layers are strategically interleaved with four fixed graph unpooling layers, allowing the network to learn representations at multiple resolutions.

We implement the technique outlined by Ranjan et al. (2018) [22] to obtain these multiple resolutions to construct pairs of pooling and unpooling layers. The process begins by estimating the pooling matrix, achieved through an iterative contraction of vertex pairs while maintaining precise surface error approximations using quadric matrices into the atlas surface mesh. Simultaneously, the unpooling matrix is derived

to enable the reversal of the pooling transformation. This process is repeated four times (in the previously pooled version of the atlas), resulting in four sets of pooling and unpooling layers, each reducing and increasing the number of nodes by a factor of two, respectively. Importantly, these pooling and unpooling matrices remain fixed during training, as they are estimated only once for the atlas surface mesh.

To increase our model’s performance, we apply the concept of deep supervision [27], which involves supervising the network at various resolution levels. During training, we utilise the estimated pooling operation to obtain down-sampled versions of the ground-truth meshes, enabling us to minimise the reconstruction error at each resolution level. Ultimately, we employ a final graph-convolutional layer, without bias and identity activation function, to predict the final vertex positions.

The incorporation of deep supervision terms leads to the following loss function:

$$\mathcal{L} = \mathcal{L}_r + \lambda_{KL}\mathcal{L}_{KL} + \lambda_{DS} \sum_{i=1}^4 \mathcal{L}_r^i, \quad (2)$$

where \mathcal{L}_{KL} is the previously defined KL term, λ_{DS} is a weighting factor, and the index i indicates the resolution level of the graph.

Mesh regularisation loss functions: To ensure smooth meshes, state-of-the-art approaches to surface mesh generation often use regularisers such as normal regularisation, edge length regularisation, and Laplacian smoothing (\mathcal{L}_{lap}), as introduced in [28], which we also incorporate. However, these existing metrics were initially designed for triangular surface meshes and, therefore, do not consider the structure of tetrahedral elements in a volumetric mesh [11]. We propose a new regularisation loss function designed to generate tetrahedral volumetric meshes to address this limitation directly. We introduce our new *tetrahedral element regularisation* loss,

$$\mathcal{L}_{ter} = \frac{1}{N_t} \sum_{i=1}^{N_t} \frac{1}{6} \sum_{j=1}^6 \left(\|\mathbf{e}_j^i\|_2 - \frac{1}{6} \left(\sum_{k=1}^6 \|\mathbf{e}_k^i\|_2 \right) \right)^2, \quad (3)$$

where N_t is the number of tetrahedra, i represents the i^{th} tetrahedron and \mathbf{e}_j^i and \mathbf{e}_k^i represent the edges of that tetrahedron. This term encourages tetrahedron regularity by penalising elements with edge lengths too different from the average edge length for each tetrahedron. Thus, the final loss function used to train the model results in

$$\mathcal{L} = \mathcal{L}_r + \lambda_{KL}\mathcal{L}_{KL} + \lambda_{DS} \sum_{i=1}^4 \mathcal{L}_r^i + \lambda_{reg}\mathcal{L}_{reg}, \quad (4)$$

where \mathcal{L}_{reg} can be any of the regularisation losses mentioned above: \mathcal{L}_{lap} for the surface case or \mathcal{L}_{ter} for the volumetric case, and λ_{reg} is the corresponding weighting factor.

III. EXPERIMENTAL SETUP

A. Data and annotations

Data for this study were collected from the UK Biobank (UKB) under access applications 2,964 and 11,350. The study adhered to the guidelines outlined in the Declaration of Helsinki and received ethical approval from the National Research Ethics Service of the National Health Service on 17 June 2011 (Ref 11/NW/0382) and extended on 10 May 2016 (Ref 16/NW/0274). Informed consent was obtained from all participants. The UKB resource is available for researchers to use for public-interest health-related research. The rationale behind the UKB imaging study is explained in Petersen *et al.* (2013) [29], and the CMR acquisition protocol is detailed in Petersen *et al.* (2015)[17].

We performed our experiments on train/test splits from 4525 UKB subjects. To ensure a fair comparison with previous work and facilitate the reproducibility of our results, we used the same train/test splits as Xia *et al.* [14], in which 600 subjects were reserved as a separate test split. This allowed us to consistently evaluate and compare the model’s performance with previous studies.

Image and mesh pre-processing: CMR images were pre-processed by normalising intensities to the range [0, 1]. SAX images had dimensions ranging from (100, 100, 6) to (200, 200, 16) and a voxel spacing of [1.82, 1.82, 10] mm, while LAX images had varying dimensions depending on the associated SAX image. To handle different sizes of SAX images between subjects, we evaluated our model in two settings: (1) *Full image input*, where we padded all SAX images to (210, 210, 16), and (2) *Cut input*, where we followed previous work [30], [14] and cropped SAX images to (100, 100, 16), padding slices as needed. In all cases, the LAX images were zero-padded to have a square shape of size (224, 224).

Inspired by classic object detection approaches, we align the vertex positions of the mesh with their relative position inside the SAX image, which is effective when using graph generative models for landmark detection [15]. We first remove the origin of the SAX image and divide each direction by the corresponding voxel spacing to obtain the positions in the voxel space. For the full-image pipeline, we add the padding applied to the positions and divide by the image size. For the cropped-image pipeline, we subtract the origin of the bounding box and divide it by the image size. With this, we obtain a *relative positional space* for training the models, with a value of (0.5, 0.5, 0.5) indicating a node in the centre of the SAX image. To evaluate the results, we reversed this operation and recovered the original positions in millimetres.

Data augmentation: All models were trained using online data enhancement, including intensity enhancement, random rotations of the SAX images (between -10 and 10 degrees), and arbitrary scaling on the x and y axes. The LAX images were scaled to match the scaling performed in the associated SAX image using each LAX image’s respective direction vector. We added a step to randomly choose the cropping centre for the cropped model, ensuring that the entire heart is always

Metrics	MCSI-Net SAX	HybridVNet		MCSI-Net SAX-LAX	MV-HybridVNet		
	Cropped	Full Image	Cropped	Cropped	Full Image	Cropped	
LV Endo	DC \uparrow	0.87 (0.05)	0.89 (0.05)	0.90 (0.04)	0.88 (0.05)	0.90 (0.04)	0.91 (0.04)
	HD \downarrow	5.13 (1.97)	4.48 (1.32)	4.08 (1.22)	4.74 (1.75)	4.22 (1.22)	3.89 (1.18)
	MCD \downarrow	1.93 (0.83)	1.67 (0.55)	1.49 (0.49)	1.86 (0.79)	1.55 (0.51)	1.39 (0.46)
LV Myo	DC \uparrow	0.76 (0.09)	0.80 (0.06)	0.83 (0.05)	0.78 (0.08)	0.81 (0.05)	0.84 (0.04)
	HD \downarrow	5.31 (1.98)	4.71 (1.36)	4.23 (1.27)	4.75 (1.76)	4.40 (1.26)	3.96 (1.23)
	MCD \downarrow	1.97 (0.95)	1.71 (0.56)	1.49 (0.51)	1.86 (0.82)	1.57 (0.52)	1.35 (0.46)
RV Endo	DC \uparrow	0.85 (0.06)	0.85 (0.05)	0.86 (0.05)	0.85 (0.06)	0.86 (0.05)	0.87 (0.05)
	HD \downarrow	7.11 (2.78)	6.97 (2.31)	6.44 (2.19)	7.06 (2.64)	6.79 (2.23)	6.13 (2.23)
	MCD \downarrow	2.34 (0.98)	2.10 (0.64)	1.90 (0.57)	2.27 (0.95)	1.99 (0.59)	1.76 (0.59)

TABLE I: Quantitative ventricle segmentation results for surface meshes. An up arrow (\uparrow) indicates that higher values are better, while a down arrow (\downarrow) indicates that lower values are better.

inside the region. This helps the model avoid dependence on a perfectly centred crop and is an extra data augmentation step.

B. Model implementation and training details

All models were implemented in Python using the PyTorch framework [31]. The PyTorch Geometric library [32] was used for the spectral graph convolutional neural network (GCNN) layers. Hyperparameters were selected through grid search, with the k hop neighbourhood parameter [25] set to 6. We conducted training for 600 epochs using the Adam optimiser with a learning rate of 10^{-4} . The batch size was set to 4, and the weight decay was applied at 10^{-5} . A KL divergence weight factor of $\lambda_{KL} = 10^{-5}$ was introduced, and a learning rate decline with a factor of 0.99 occurred after each epoch. The 2D and 3D Convolutional Neural Network (CNN) encoders consisted of six residual blocks [33]. In 2D encoders, the maxpooling layers were interleaved with these blocks. In 3D encoders, max-pooling was applied on the X and Y axes between each residual block, with Z-axis max-pooling at the third layer. After a grid search hyperparameter selection, the latent representations were obtained using fully connected layers in the encoders, with a dimension of 32 for the 3D encoder and 8 for all 2D encoders. GCNN decoders, in both 2D and 3D models, comprised six layers of Chebyshev convolutions with Layer Normalisation [26] and ReLU nonlinearities. Classic surface regularisation losses from the PyTorch3D library [34] were used. These losses included edge length, normal vector, and Laplacian regularisation terms.

C. Model comparison

We implemented different single- and multiview variants of the HybridVNet architecture. We also compared our approach with the results obtained by the Multi-Cue Shape Inference Network (MCSI-Net) [14] for the dense segmentation task of the ventricle, which constitutes the state-of-the-art point distribution models in this particular data set. MCSI-Net combines two different networks. The first is a position-inference network that predicts the central coordinates of the mesh and a rotation vector. The second is a shape-inference network that uses CNN layers to infer the parameters of a point distribution model (PDM) based on PCA. This model uses the same SAX

and multiple LAX views as ours, but also incorporates patient metadata information into the PDM learning process. On the contrary, our model does not require patient metadata.

IV. RESULTS AND DISCUSSION

We conducted a comprehensive series of experiments to evaluate the performance of the proposed HybridVNet model alongside the baseline models and their various configurations. These experiments covered surface and tetrahedral volumetric mesh scenarios, including a sensitivity analysis of the proposed regularisation losses. All evaluations were carried out on the same test dataset comprising 600 subjects, as presented in Xia *et al.* 2022 [14], for the ground truth meshes associated with this dataset.

A. Surface mesh extraction

To evaluate the quality of cardiac meshes, we used mesh metrics (II) and mask-based metrics (Table I). First, to enable a direct comparison MCSI-Net, which was evaluated directly on the segmentation masks generated by the model in the SAX image space, we derived dense segmentation masks from the surface meshes. Then, we evaluated classic segmentation metrics such as Dice coefficient, Hausdorff distance, and the average distance between the reference and predicted contours in each slice.

In our initial comparison, we evaluated our HybridVNet against the SAX-only MCSI-Net with full images and cropped versions centred on the structure of interest (Table I). Remarkably, HybridVNet outperforms SAX MCSI-Net for all metrics and structures. Next, we compare our MV-HybridVNet with the standard MCSI-Net, which also incorporates multiple views and is the current state of the art for this data set. The results demonstrate the superiority of our MV-HybridVNet, as it outperforms the standard MCSI-Net across all segmentation metrics for both the left and right ventricle segmentation tasks.

Our *full image* variant of the model achieves better results compared to the baselines, all while eliminating the need for an additional step to detect the region of interest (ROI) during the segmentation process. Furthermore, the MV-HybridVNet model on *cropped images* beats the results with significant differences relative to the full image.

Subpart	Metric	Full SAX Image		Cropped SAX Image	
		HybridVNet	MV-HybridVNet	HybridVNet	MV-HybridVNet
Full Mesh	MAE ↓	2.56 (0.62)	2.26 (0.55)	2.43 (0.59)	2.18 (0.54)
	MSE ↓	12.20 (7.11)	9.29 (5.48)	11.27 (6.69)	8.80 (5.31)
	RMSE ↓	3.38 (0.89)	2.95 (0.76)	3.25 (0.86)	2.87 (0.76)
LV	MAE ↓	1.90 (0.57)	1.79 (0.55)	1.75 (0.54)	1.70 (0.54)
	MSE ↓	6.23 (4.28)	5.60 (4.03)	5.35 (3.83)	5.11 (3.67)
	RMSE ↓	2.39 (0.73)	2.26 (0.71)	2.21 (0.70)	2.15 (0.70)
RV	MAE ↓	2.18 (0.64)	2.08 (0.60)	2.00 (0.58)	1.97 (0.59)
	MSE ↓	8.39 (5.64)	7.69 (4.93)	7.12 (4.84)	7.04 (4.72)
	RMSE ↓	2.78 (0.82)	2.66 (0.78)	2.56 (0.76)	2.54 (0.78)
LA	MAE ↓	2.90 (1.00)	2.37 (0.78)	2.84 (0.99)	2.30 (0.77)
	MSE ↓	15.40 (13.73)	10.07 (9.74)	14.88 (13.29)	9.58 (9.24)
	RMSE ↓	3.69 (1.33)	3.00 (1.02)	3.63 (1.31)	2.92 (1.02)
RA	MAE ↓	3.07 (0.96)	2.57 (0.76)	2.98 (0.93)	2.51 (0.80)
	MSE ↓	17.46 (13.65)	12.00 (9.42)	16.67 (13.13)	11.75 (10.16)
	RMSE ↓	3.97 (1.32)	3.30 (1.05)	3.87 (1.30)	3.24 (1.11)
AORTA	MAE ↓	2.66 (0.93)	2.37 (0.84)	2.56 (0.89)	2.34 (0.83)
	MSE ↓	13.17 (11.05)	10.24 (8.71)	12.38 (10.52)	10.04 (8.43)
	RMSE ↓	3.41 (1.23)	3.01 (1.09)	3.31 (1.20)	2.97 (1.09)

TABLE II: Quantitative mesh evaluation results for surface meshes. An up arrow (\uparrow) indicates that higher values are better, while a down arrow (\downarrow) indicates that lower values are better.

To account for structures that may not be visible in SAX images and to provide more insight into how the incorporation of long-axis views in our model helps the model learn more details about the complete heart structure, we conducted a thorough evaluation of our proposed models directly on various subparts of the output mesh. Standard mesh evaluation metrics, including vertex mean squared error (MSE), mean average error (MAE) and root mean squared error (RMSE), were calculated in millimetres. Table II summarises the results in our models, comparing HybridVNet with its multiview version for *cropped images* and *full images* versions independently. Evaluation was performed at the nodes of the left ventricle (LV), right ventricle (RV), left atrium (LA), right atrium (RA) and aorta.

Comparing the performance of the HybridVNet with and without the inclusion of LAX images, we observed a significant improvement in accuracy for all parts of the mesh. This improvement is particularly pronounced for the left and right atria (LA and RA) and the aorta, which are not fully visible in SAX images. The base HybridVNet model demonstrates the ability to approximate the positions of these structures, with further refinement achieved through the integration of LAX images.

Surface mesh regularisation effect: In the context of the surface mesh experiment, we performed a comprehensive evaluation of various surface regularisation loss functions to enhance the performance of our HybridVNet model. Specifically, we investigated the efficacy of three distinct regularisation approaches: normal regularisation, edge-length regularisation, and Laplacian smoothing. For more information on these regularisers, see [28].

Notably, while commonly employed in mesh regularisation

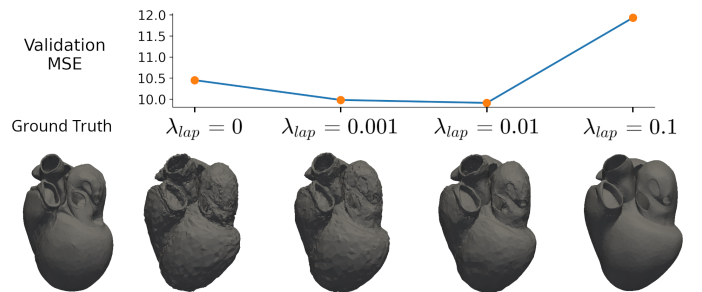


Fig. 2: Qualitative analysis of the impact of Laplacian regularisation term on surface mesh smoothness. It demonstrates the influence of adjusting the regularisation parameter on mesh quality. The best quantitative results regarding MSE for the validation split were achieved when $\lambda_{lap} = 0.01$.

tasks, normal regularisation, and edge length regularisation did not yield significant improvements in our model’s performance. This observation aligns with the intuitive understanding that these metrics are better suited for meshes with varying node counts and highly irregular target shapes. This is not the case in our dataset. In contrast, the incorporation of Laplacian smoothing produced notably smoother surface meshes. This can be visually appreciated in Figure 2, which presents a qualitative analysis of the meshes obtained as the regularisation parameter for the Laplacian regularisation loss was increased. Figures clearly illustrate the enhanced smoothness and quality of the meshes as the regularisation strength is adjusted.

To assess the impact of different loss terms during the training process, we refer to Figure 3. This figure provides a comparison of the MSE values throughout both the training

Metrics		MV-HybridVNet			
		$\lambda_{ter} = 0$	$\lambda_{ter} = 1E-4$	$\lambda_{ter} = 1E-3$	$\lambda_{ter} = 1E-2$
Mesh	MAE ↓	2.08 (0.63)	2.07 (0.64)	2.04 (0.61)	2.11 (0.61)
	MSE ↓	8.25 (6.14)	8.22 (6.12)	7.93 (5.63)	8.39 (6.00)
	RMSE ↓	2.74 (0.88)	2.73 (0.88)	2.69 (0.84)	2.77 (0.84)
LV Endo	DC ↑	0.90 (0.04)	0.90 (0.04)	0.90 (0.05)	0.88 (0.05)
	HD ↓	4.36 (1.22)	4.32 (1.24)	4.41 (1.35)	5.21 (1.42)
	MCD ↓	1.52 (0.46)	1.51 (0.49)	1.58 (0.54)	1.89 (0.62)
LV Myo	DC ↑	0.78 (0.04)	0.78 (0.04)	0.76 (0.05)	0.74 (0.06)
	HD ↓	5.27 (1.47)	4.98 (1.40)	5.17 (1.50)	5.30 (1.57)
	MCD ↓	1.86 (0.61)	1.81 (0.64)	1.95 (0.72)	1.96 (0.77)
RV Endo	DC ↑	0.85 (0.06)	0.86 (0.05)	0.85 (0.05)	0.85 (0.06)
	HD ↓	7.22 (2.76)	6.97 (2.54)	7.38 (2.67)	7.55 (2.80)
	MCD ↓	2.05 (0.64)	2.02 (0.63)	2.09 (0.64)	2.13 (0.69)

TABLE III: Quantitative results for segmentation metrics in volumetric meshes. (↑) indicates that higher results are better, while (↓) indicates that lower results are better. Bold results in two columns indicate there are no significant differences between these two.

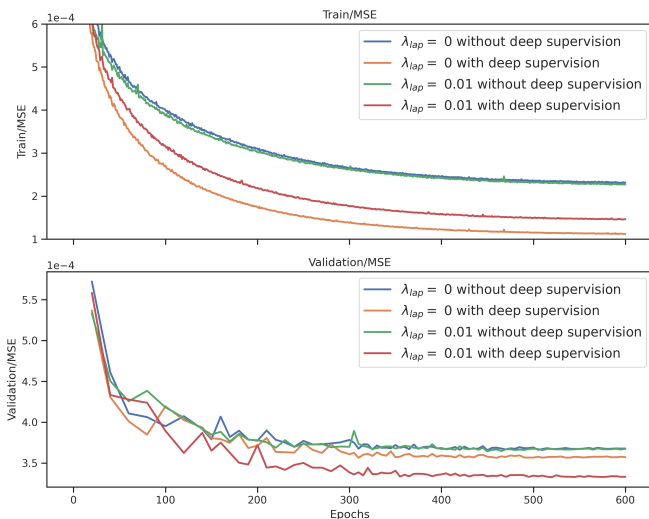


Fig. 3: MSE values throughout training and validation for different configurations of hyperparameters, measured in the *relative positional space*. The red curve highlights the significant impact of combining deep supervision and Laplacian regularisation losses on model performance. Smaller intervals were used for loss recording as training progressed.

and validation phases. Notably, due to the resource-intensive nature of the validation process, we adjusted the intervals when recording loss values, with smaller intervals as more training time elapsed.

Significantly, the red curve in Figure 3 illustrates that the best performance is achieved when combining both deep supervision and Laplacian regularisation losses. This combination eases the training process and leads to improved model performance. The optimal regularisation strength for Laplacian smoothing, resulting in the best MSE for the entire image and cropped models, was determined to be $\lambda_{lap} = 0.01$. This finding was consistent with both qualitative and quantitative

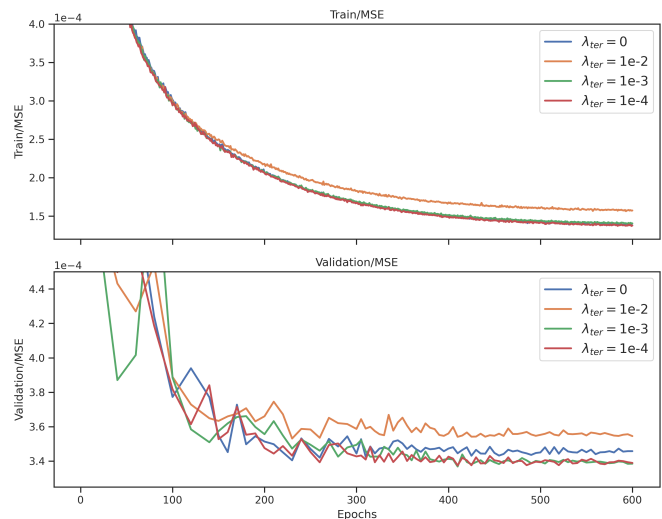


Fig. 4: MSE values throughout training and validation for volumetric meshes, exploring different configurations of λ_{ter} , with values measured in the *relative positional space*. Noticeably, $\lambda_{ter} = 1E-2$ (Yellow) shows a high-performance decay for both train and validation curves. Smaller intervals were used for loss recording as training progressed.

evaluations, as over-smoothed meshes appeared when using high values of the regularisation term.

B. Towards simulation-ready tetrahedral meshes

Our second experiment focused on the creation of simulation-ready tetrahedral meshes. We evaluated various weighting factors (λ_{ter}) for the term of regularisation of the tetrahedral element defined in (3), to understand its influence on both the quality of the mesh and the performance of ventricle segmentation. Table III presents the results, including metrics for mesh quality and ventricle segmentation, in different λ_{ter} values.

		Mean	Std	Min	Max	1%	5%	25%	50%	75%
Reference Meshes	Atlas	0.491	0.174	0.092	0.984	0.115	0.194	0.367	0.494	0.617
	Ground Truth	0.355	0.156	-0.207	0.838	0.04	0.103	0.238	0.353	0.47
	Simpleware	0.524	0.185	0.064	0.992	0.128	0.202	0.387	0.535	0.667
MV-HybridGNet3D	$\lambda_{ter} = 0$	0.222	0.225	-0.759	0.876	-0.327	-0.144	0.065	0.219	0.384
	$\lambda_{ter} = 1E-4$	0.229	0.23	-0.771	0.871	-0.337	-0.151	0.068	0.231	0.397
	$\lambda_{ter} = 1E-3$	0.433	0.206	-0.719	0.904	-0.138	0.059	0.307	0.457	0.585
	$\lambda_{ter} = 1E-2$	0.501	0.309	-0.931	0.943	-0.681	-0.298	0.434	0.577	0.688

TABLE IV: Quantitative results for the quality of elements in volumetric meshes. The values correspond to the scaled Jacobian, and higher values imply a better quality of the tetrahedra.

Our exploration reveals a nuanced relationship between λ_{ter} and the model’s performance. In particular, the best outcomes emerge for segmentation metrics when $\lambda_{ter} = 1E-4$. In this configuration, the results closely resemble the non-regularised model, especially concerning the LV Endo metrics. However, for metrics related to mesh prediction performance, the optimal choice changes slightly, with $\lambda_{ter} = 1E-3$ yielding the best outcomes. Although this setting leads to a minor drop in ventricle segmentation performance, it significantly reduces the mesh error.

A closer examination of the training dynamics, as illustrated in Figure 4, reinforces the benefits of using small values of λ_{ter} . These values result in improved validation performance without substantial fluctuations in the training curves. On the contrary, the highest regularisation strength ($\lambda_{ter} = 1E-2$) leads to decreased performance in both training and validation. Note that the impact of the regularisation term on the ventricle segmentation metrics reported is not drastic. However, as demonstrated in Figure 5 and elaborated in the following paragraphs, it substantially increases the quality of tetrahedral elements, a critical consideration for simulations.

We used the widely adopted scaled Jacobian metric to validate the quality of tetrahedral elements. The Jacobian of a tetrahedron is a matrix that describes how the tetrahedron’s shape changes under deformation. The scaled Jacobian is a quantitative measure of regularity and symmetry, falling within the range $[-1, 1]$ and not affected by scale or units. A high-scaled Jacobian value implies high regularity, low distortion, and therefore high quality [35]. Table IV provides a comprehensive overview of element quality under different λ_{ter} conditions. The table includes statistics such as the average, standard deviation, minimum, maximum, and various percentiles of the quality of tetrahedron in all test subjects. We compare our approaches with volumetric atlases, ground truth meshes, and a subset of surface meshes converted to volumetric meshes using Simpleware’s ScanIP [20].

Importantly, these findings demonstrate that our regularised models surpass ground-truth elements in terms of quality, beginning from the 25% quartile and onwards, for $\lambda_{ter} = 1E-3$ and higher. This observation underscores our hypothesis that the regularisation loss significantly enhances the mesh quality. Figure 5 visually summarises this improvement, positioning our method competitively with Simpleware meshes, except for a small number of elements, potentially due to the original low quality of the ground truth.

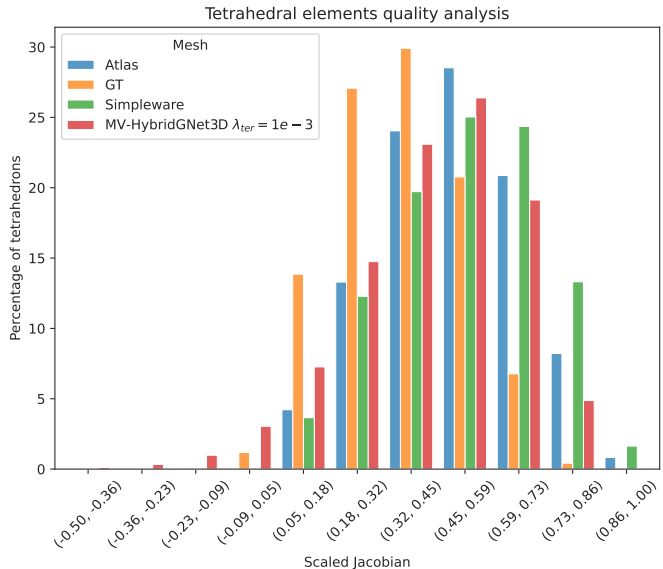


Fig. 5: Histogram of tetrahedral mesh quality using scaled Jacobian values. The x-axis represents the scaled Jacobian values, and the y-axis shows the percentage of tetrahedral elements within each range.

Overall, our model demonstrates competitive results compared to the conventional approach of directly converting surface to volumetric meshes. Moreover, it addresses a challenge posed by direct conversion, where degenerate triangles can obstruct the creation of volumetric meshes, affecting approximately 10% of cases in our experiments. When comparing the time required for generating a volumetric mesh, Simpleware’s ScanIP procedure consumes approximately 6 minutes on average for each mesh, employing the same configuration as used in the atlas generation procedure. In contrast, our approach requires less time for generating the vertex set of volumetric meshes. When executed on an NVIDIA A100-SXM4 GPU, it accomplishes this task in just 0.04 seconds for each set of CMR images during the forward pass, resulting in a substantial speed improvement. Even in cases where GPU computing is unavailable, when running on an Intel(R) Core(TM) i7-7700 CPU operating at 3.60GHz, the forward pass requires only 5 seconds on average, providing a significant acceleration.

V. CONCLUSIONS

This study introduces HybridVNet, a novel method for directly generating surface and tetrahedral meshes from images. Our comprehensive experiments and evaluations reveal that HybridVNet significantly enhances mesh accuracy and versatility compared to state-of-the-art point distribution models that depend on linear PCA component decoding. In particular, integrating short- and long-axis views has yielded improved results, capturing finer details of the complete cardiac structure. HybridVNet stands out for its efficiency and speed, substantially reducing vertex set generation time compared to conventional approaches, a precious trait for large-scale processing such as in studies on the UK Biobank. The generic nature of HybridVNet opens doors to broader applications in medical image analysis, with potential extensions to tasks such as cortical surface reconstruction from brain magnetic resonance images. Future work will direct efforts toward enhancing the element quality of the tetrahedral ground truth used for model training, ensuring more accurate evaluations of our method's potential for in-silico simulation-based studies.

REFERENCES

- [1] M. Fedele and A. Quarteroni, "Polygonal surface processing and mesh generation tools for the numerical simulation of the cardiac function," *International Journal for Numerical Methods in Biomedical Engineering*, vol. 37, no. 4, p. e3435, 2021.
- [2] R. Bonazzola, N. Ravikumar, R. Attar, E. Ferrante, T. Syeda-Mahmood, and A. F. Frangi, "Image-derived phenotype extraction for genetic discovery via unsupervised deep learning in CMR images," in *MICCAI*. Springer, 2021, pp. 699–708.
- [3] M. Beetz, J. C. Acero, A. Banerjee, I. Eitel, E. Zacur, T. Lange, T. Stiermaier, R. Evertz, S. J. Backhaus, H. Thiele, A. Bueno-Orovio, P. Lamata, A. Schuster, and V. Grau, "Mesh u-nets for 3d cardiac deformation modeling," in *Statistical Atlases and Computational Models of the Heart. Regular and CMRxMotion Challenge Papers*, O. Camara, E. Puyol-Antón, C. Qin, M. Sermesant, A. Suinesiaputra, S. Wang, and A. Young, Eds. Cham: Springer Nature Switzerland, 2022, pp. 245–257.
- [4] S. Ordas, E. Oubel, R. Leta, F. Carreras, and A. F. Frangi, "A statistical shape model of the heart and its application to model-based segmentation," in *Medical Imaging 2007: Physiology, Function, and Structure from Medical Images*, vol. 6511. SPIE, 2007, pp. 490–500.
- [5] W. Bai, W. Shi, C. Ledig, and D. Rueckert, "Multi-atlas segmentation with augmented features for cardiac mr images," *Medical image analysis*, vol. 19, no. 1, pp. 98–109, 2015.
- [6] A. Neic, M. A. Gsell, E. Karabelas, A. J. Prassl, and G. Plank, "Automating image-based mesh generation and manipulation tasks in cardiac modeling workflows using meshtool," *SoftwareX*, vol. 11, p. 100454, 2020.
- [7] O. Ronneberger, P. Fischer, and T. Brox, "U-net: Convolutional networks for biomedical image segmentation," in *MICCAI*. Springer, 2015, pp. 234–241.
- [8] F. Milletari, N. Navab, and S.-A. Ahmadi, "V-net: Fully convolutional neural networks for volumetric medical image segmentation," in *2016 fourth international conference on 3D vision (3DV)*. IEEE, 2016, pp. 565–571.
- [9] A. J. Larrazabal, C. Martínez, B. Glocker, and E. Ferrante, "Post-dae: anatomically plausible segmentation via post-processing with denoising autoencoders," *IEEE TMI*, 2020.
- [10] E. Puyol-Anton *et al.*, "A multimodal spatiotemporal cardiac motion atlas from mr and ultrasound data," *Medical image analysis*, vol. 40, pp. 96–110, 2017.
- [11] D. H. Pak, M. Liu, T. Kim, L. Liang, R. McKay, W. Sun, and J. S. Duncan, "Distortion energy for deep learning-based volumetric finite element mesh generation for aortic valves," in *MICCAI*. Springer International Publishing, 2021, pp. 485–494.
- [12] F. Kong and S. C. Shadden, "Whole heart mesh generation for image-based computational simulations by learning free-from deformations," in *MICCAI*. Springer, 2021, pp. 550–559.
- [13] K. Tóthová, S. Parisot, M. Lee, E. Puyol-Antón, A. King, M. Pollefeys, and E. Konukoglu, "Probabilistic 3D surface reconstruction from sparse MRI information," in *International Conference on Medical Image Computing and Computer-Assisted Intervention*. Springer, 2020, pp. 813–823.
- [14] Y. Xia *et al.*, "Automatic 3D+t four-chamber CMR quantification of the UK biobank: integrating imaging and non-imaging data priors at scale," *Medical Image Analysis*, vol. 80, p. 102498, 2022.
- [15] N. Gaggion, L. Mansilla, C. Mosquera, D. H. Milone, and E. Ferrante, "Improving anatomical plausibility in medical image segmentation via hybrid graph neural networks: applications to chest x-ray analysis," *IEEE Transactions on Medical Imaging*, 2022.
- [16] N. Gaggion, L. Mansilla, D. H. Milone, and E. Ferrante, "Hybrid graph convolutional neural networks for landmark-based anatomical segmentation," in *MICCAI*. Springer International Publishing, 2021.
- [17] S. E. Petersen *et al.*, "UK biobank's cardiovascular magnetic resonance protocol," *Journal of cardiovascular magnetic resonance*, vol. 18, no. 1, pp. 1–7, 2015.
- [18] C. Rodero *et al.*, "Linking statistical shape models and simulated function in the healthy adult human heart," *PLOS Computational Biology*, vol. 17, no. 4, pp. 1–28, 04 2021.
- [19] S. E. Petersen, N. Aung, M. M. Sanghvi, F. Zemrak, K. Fung, J. M. Paiva, J. M. Francis, M. Y. Khanji, E. Lukaschuk, A. M. Lee *et al.*, "Reference ranges for cardiac structure and function using cardiovascular magnetic resonance (cmr) in caucasians from the uk biobank population cohort," *Journal of cardiovascular magnetic resonance*, vol. 19, no. 1, pp. 1–19, 2017.
- [20] Synopsys, "Simpleware," 2021, <https://www.synopsys.com/simpleware.html>, Last opened on 2023-11-08.
- [21] M. Musy and others., "vedo: 2022.4.1," Oct. 2022.
- [22] A. Ranjan, T. Bolkart, S. Sanyal, and M. J. Black, "Generating 3D faces using convolutional mesh autoencoders," in *Proceedings of the European Conference on Computer Vision (ECCV)*, 2018, pp. 704–720.
- [23] K. He, X. Zhang, S. Ren, and J. Sun, "Deep residual learning for image recognition," in *Proceedings of the IEEE conference on computer vision and pattern recognition*, 2016, pp. 770–778.
- [24] D. P. Kingma and M. Welling, "Auto-encoding variational bayes," *arXiv preprint arXiv:1312.6114*, 2013.
- [25] M. Defferrard, X. Bresson, and P. Vandergheynst, "Convolutional neural networks on graphs with fast localized spectral filtering," *arXiv preprint arXiv:1606.09375*, 2016.
- [26] J. L. Ba, J. R. Kiros, and G. E. Hinton, "Layer normalization," *arXiv preprint arXiv:1607.06450*, 2016.
- [27] C.-Y. Lee, S. Xie, P. Gallagher, Z. Zhang, and Z. Tu, "Deeply-supervised nets," in *Artificial intelligence and statistics*, 2015, pp. 562–570.
- [28] N. Wang, Y. Zhang, Z. Li, Y. Fu, W. Liu, and Y.-G. Jiang, "Pixel2mesh: Generating 3D mesh models from single rgb images," in *Proceedings of the European conference on computer vision (ECCV)*, 2018, pp. 52–67.
- [29] S. E. Petersen *et al.*, "Imaging in population science: cardiovascular magnetic resonance in 100,000 participants of UK Biobank - rationale, challenges and approaches," *Journal of Cardiovascular Magnetic Resonance*, vol. 15, no. 1, p. 46, Dec. 2013.
- [30] R. Attar *et al.*, "Quantitative CMR population imaging on 20,000 subjects of the UK biobank imaging study: Lv/rv quantification pipeline and its evaluation," *Medical image analysis*, vol. 56, pp. 26–42, 2019.
- [31] A. Paszke *et al.*, "Pytorch: An imperative style, high-performance deep learning library," in *Advances in Neural Information Processing Systems*, 2019.
- [32] M. Fey and J. E. Lenssen, "Fast graph representation learning with PyTorch Geometric," in *ICLR Workshop on Representation Learning on Graphs and Manifolds*, 2019.
- [33] K. He, X. Zhang, S. Ren, and J. Sun, "Deep residual learning for image recognition," in *2016 IEEE Conference on Computer Vision and Pattern Recognition (CVPR)*, 2016, pp. 770–778.
- [34] N. Ravi *et al.*, "Accelerating 3D deep learning with pytorch3d," *arXiv:2007.08501*, 2020.
- [35] A. Johnen, C. Geuzaine, T. Toulorge, and J.-F. Remacle, "Efficient computation of the minimum of shape quality measures on curvilinear finite elements," *Computer-Aided Design*, vol. 103, pp. 24–33, 2018.